Scattering of Inertial Waves by an Ocean Front

DAVID M. RUBENSTEIN

Science Applications International Corporation, McLean, VA 22102

GLYN O. ROBERTS

Roberts Associates, Incorporated, 1726 Pine Valley Dr., Vienna, VA 22180

(Manuscript received 4 February 1985, in final form 29 July 1985)

ABSTRACT

Recent observations suggest that the space–time spectrum of near-inertial motions is strongly modulated by ocean fronts and geostrophic shear. This paper postulates a mechanism that may be responsible for generating much of this variability in the vicinity of fronts. The effective inertial frequency is variable because of gradients in the mean flow associated with a front. As a result, phase differences accumulate in inertial oscillations over short length scales of order tens of kilometers. Inertial pumping ensues, and near-inertial waves propagate away from the front in various directions. Inertial energy in the mixed layer disperses more rapidly in the vicinity of the front, and the mixed layer depth assumes strong across-front variations. In the thermocline, scattered internal waves develop a modulated pattern of amplitude, within the front and in its vicinity.

In order to investigate this mechanism, a two-dimensional numerical model is developed. The model simulates a mixed layer sitting over a stratified interior, and a barotropic jet. Solutions are suggestive of patterns of variability that have been observed in the ocean.

1. Introduction

Much of the energy in the near-inertial frequency band is known to result from wind-induced surface forcing. It is puzzling, then, that so many investigators have found that the horizontal coherence scale of near-inertial waves is much smaller than typical storm scales. Length scales on the order of a few tens of kilometers are typical (Webster, 1968; Schott, 1971; Pollard, 1980; Fu, 1981). It is important to understand the mechanisms that produce these shorter scales, because small horizontal scale inertial waves transfer energy much more rapidly than do large scale waves.

Weller (1982) analyzed the inertial oscillations observed in the mixed layer during the Joint Air–Sea Interaction project of 1978. He showed that oscillations measured by two moorings were not laterally coherent. According to Weller, this spatial variability was caused by horizontal shears associated with the mean flow. Mean flow that has vorticity will shift the effective inertial frequency. Mean flow that is convergent or divergent will cause inertial oscillations to grow or decay.

The question that arises is how spatial variability—arising from mean flow in the mixed layer—affects the transfer of near-inertial energy to the thermocline. There is some evidence for strong spatial variability of inertial waves in the vicinity of a mesoscale front (Kunze and Sanford, 1984, Mied et al., 1985). However, the evidence is still meager, largely because most observations of near-inertial waves are made using current meters, which are not well-suited to the measurement of horizontal variability.

Kunze (1985) and Kunze and Sanford (1984) presented the results of a ray tracing study. They allowed inertial waves of the prescribed frequency and wavenumber to propagate from the surface and to interact with a model front and an associated baroclinic jet. Rays that originated over the warm side of the front were trapped in a trough of negative vorticity. Rays originating outside the front or over the cold side were either refracted or reflected. The results suggest significant spatial variability, although the amplitude could not be predicted. In forcing their model, Kunze and Sanford chose initial vertical and horizontal wavelengths of 100 m and 40 km, respectively. These scales are comparable to the respective length scales of the model front. It might have been more realistic to have used larger initial wavelengths—especially a larger horizontal wavelength—in order to simulate the length scales appropriate to atmospheric forcing. However, the inhomogeneity scales would then have been much smaller than the wave scales, and the ray tracing approach would have been invalid.

In addition, it is not clear how small horizontal-scale inertial waves might be generated in the first place. In Section 2 of this paper, we discuss the interaction of near-inertial oscillations with a mesoscale flow field in the mixed layer. A model shows how, several inertial periods after the passage of a storm, inertial pumping might be produced over short length scales. Although

the model is rather simple, it sheds light on a physical process that may have great import on the mechanism of energy transfer in the ocean.

In Section 3 we present the equations for a new dynamical model, and we outline the numerical method of solution. The model treats the mixed layer as a vertically homogeneous slab, sitting over an inviscid stratified interior. Accompanying an ocean front, a barotropic jet is prescribed as a mean flow. Near-inertial oscillations in the mixed layer are initially homogeneous. As time elapses, these oscillations interact with the mean flow. Inhomogeneities develop, and inertial pumping induces internal waves. In Section 4 we analyze the interactions between near-inertial waves and a mean flow. We discuss these results and their implications in Section 5.

2. The effect of mean flow on inertial oscillations in the mixed layer

We begin by considering the mixed layer response to the passage of a synoptic-scale atmospheric front. The along-front length scale is on the order of hundreds or thousands of kilometers, but the across-front length scale is several tens of kilometers. If the front propagation is fast, that is, if the wind veering is sufficiently sudden with respect to an inertial period, then inertial oscillations with significant amplitudes may be generated. Most of the near-inertial energy is initially excited in the ocean mixed layer. The horizontal wavelength of these oscillations is equal to the distance traversed by the storm in an inertial period. This distance, at midlatitudes, is typically on the order of hundreds of kilometers.

This simple scenario becomes more complicated by the introduction of a mean flow with spatial variability in the mixed layer. We consider a mean flow with a scale of variability on the order of tens of kilometers. Because the initial wavelength of the inertial oscillations is much longer than this scale, we assume that the initial wavelength is infinite. In other words, a storm traveling exceedingly fast deposits momentum essentially simultaneously everywhere in the vicinity of the mean flow. Therefore our initial condition is a homogeneous wind-induced flow $h(\bar{u}_0, \bar{v}_0)$ in the mixed layer. The overbars denote depth-averaged quantities, and h is the mixed layer depth.

We consider a mean flow in geostrophic balance

$$fV = P_x, \qquad (2.1)$$

to be a basic state, where V is a function of x only. The equations for small disturbance flows $\bar{u}(x, t)$ and $\bar{v}(x, t)$ in a shallow surface layer of depth $h(x, t)$ are

$$\bar{u}_t - f\bar{v} = 0,$$

$$\bar{v}_t + f\bar{u} + \bar{u}V_x = 0,$$

$$h_t + \bar{u}h_x = -h\bar{u}_x, \qquad (2.2a\text{-}c)$$

where the overbars denote values in the layer. In a deep unstratified ocean of total depth D, the flows below the surface layer are smaller by a factor h/D, and vanish in the limit as D goes to infinity. Thus the horizontal pressure gradient is negligible in the surface layer. By linearizing (2.2a, b) we are able to compute analytic solutions for $\bar{u}$ and $\bar{v}$. We retain nonlinear terms in (2.2c) because h is a passive variable, and a numerical solution of (2.2c) shows some extremely interesting effects. These equations are discussed here primarily for illustrative purposes. A more complete justification would use the equations of Section 3, for the special case of an unstratified interior, and in the limit of infinite D.

The solution for $\bar{v}$ is

$$\bar{v}(x, t) = \bar{v}_0 \cos f_e t - (f_e/f)\bar{u}_0 \sin f_e t, \qquad (2.3)$$

where

$$f_e(x) = [f(f + V_x)]^{1/2} \qquad (2.4)$$

is an effective inertial frequency. For realistic mean flows in midlatitudes, $|V_x| \ll f$, therefore $f_e \approx f + \frac{1}{2} V_x$.

Figure 1 shows a model sinusoidal jet

$$V(x) = \begin{cases} -V_0[1 + \cos(2\pi x/\lambda)], & |x| < \lambda/2 \\ 0, & |x| \geq \lambda/2, \end{cases} \qquad (2.5)$$

where $V_0 = 15$ cm s^{-1} and $\lambda = 80$ km, and the associated function $f_e(x)/f$, where $f = 10^{-4}$ s^{-1}. Using this function, the solution (2.3), (2.4) was computed for $(\bar{u}_0, \bar{v}_0) = (0, 20)$ cm s^{-1}. Figure 2 shows this solution at periodic intervals.

The regime of the jet has a variable f_e, so that as time elapses a phase difference accumulates. This phase accumulation has no upper bound. As a result, after the passage of a storm the $\bar{u}$ and $\bar{v}$ variations take on progressively smaller length scales.

From the one-dimensional version of Lighthill's (1978) equation

$$\frac{\partial k}{\partial t} + \frac{\partial \omega}{\partial k} \frac{\partial k}{\partial x} = -\frac{\partial \omega}{\partial x} \qquad (2.6)$$

for wavenumber k and frequency ω, we find that

$$k = -\frac{t}{2} V_{xx}. \qquad (2.7)$$

In other words, the wavenumber amplitude increases linearly with time.

We computed the solution to (2.2c) numerically. Figure 3 shows contours of mixed layer depth perturbations $h(x, t) - H$, where $H = 50$ m is the initial depth. The character of this solution is striking. In the mean flow region, advection $\bar{u} \, \partial h/\partial x$ results in a tendency for $|h|$ to increase. The nonlinear advection also carries the variability in h out 10 km beyond either side of the mean flow region. Whereas the wavelength of the $f_e(x)$ distribution is 80 km, significant variability in h is generated over a 40 km wavelength.
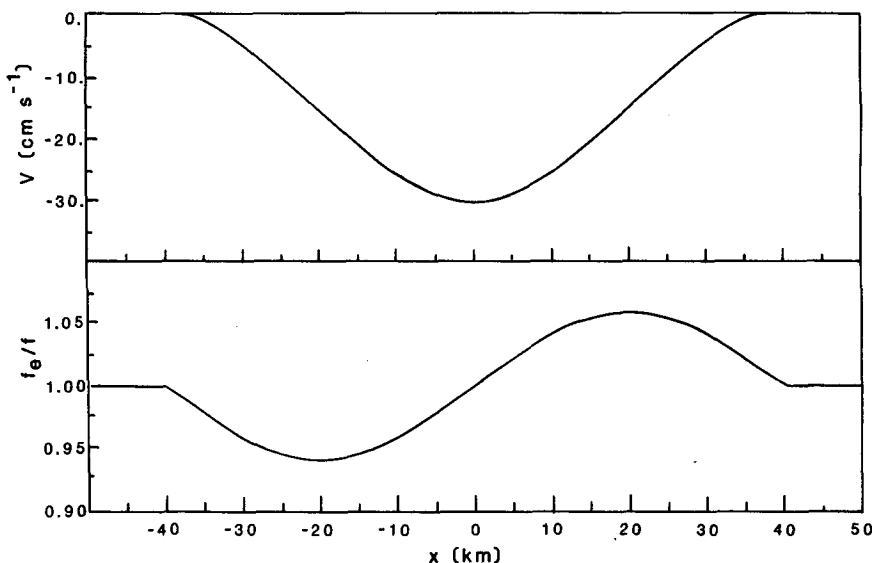
FIG. 1. A model jet in the mixed layer, and the associated effective inertial frequency
given by $f_e = [f(f + V_x)]^{1/2}$.

Trial computations were also performed with various initial mixed layers, $H = 25$ and 100 m. Keeping in mind the conservation of momentum, the initial velocity perturbations for these cases were $\bar{v}_0 = 40$ and 10 cm s^{-1}, respectively. Because the solutions are qualitatively similar, they are not displayed here. The initially deeper mixed layers develop variability at a slower rate. In quantitative terms, the degree of variability achieved in Fig. 3 for $H = 50$ m after 5 inertial periods is achieved after about 3 and 7 inertial periods for

$H = 25$ and 100 m, respectively. The point to keep in mind is that these cases continue to accumulate variability indefinitely.

In the real ocean, of course, this proliferation of scales cannot continue indefinitely. Before nonlinear effects become important, divergence of the $\bar{u}$ field produces inertial pumping. Vertical motions over small horizontal length scales excite near-inertial internal waves that are free to propagate down into the thermocline. In this manner, energy radiates out of the mixed layer,
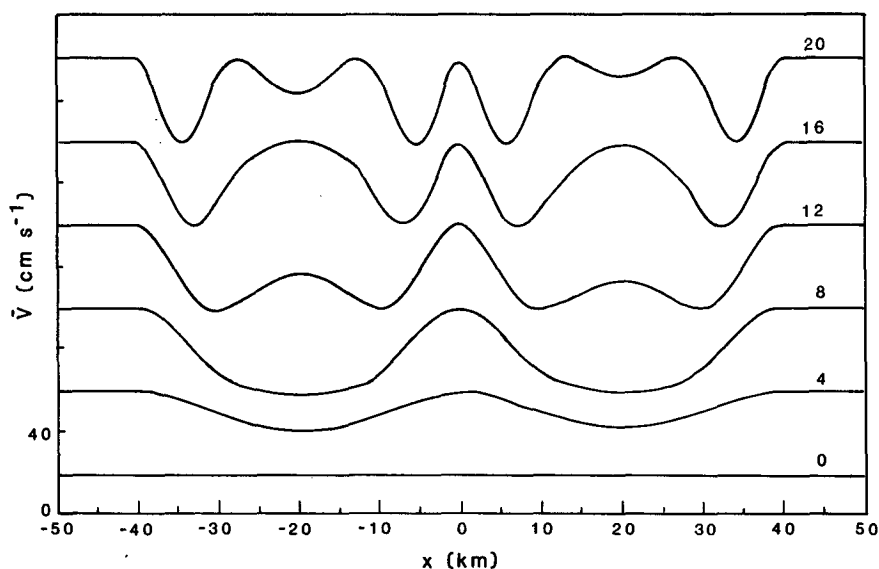
FIG. 2. The model solutions for $\bar{v}$ given by (2.3). The initial condition is $\bar{v} = 20$ cm s^{-1}. Solutions are shown at 4-inertial-period intervals, and are successively displaced by 40 cm s^{-1}. Note that as time elapses, the significant length scales decrease.
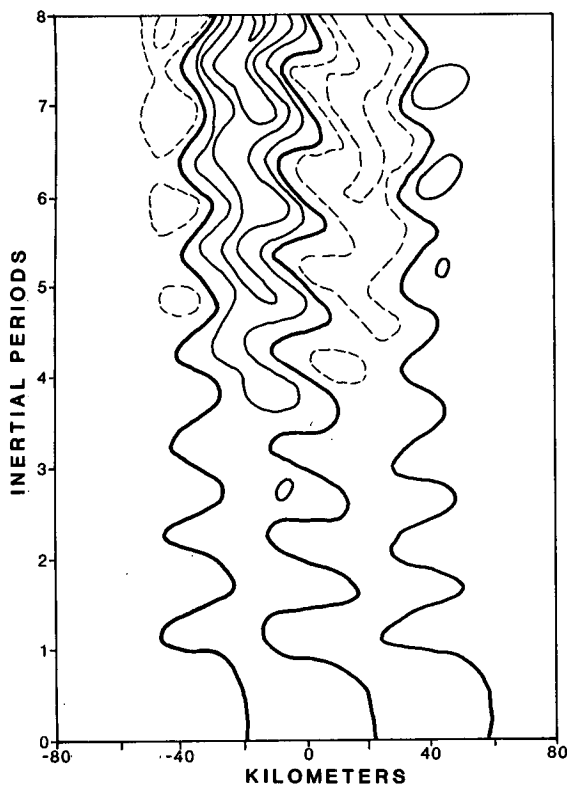
FIG. 3. Mixed layer depth perturbations $h(x, t) - H$, where H = 50 m. Contour increment is 6 m. Dashed curves denote negative perturbations. The thick curves denote zero contours. In this solution, for an unstratified interior, variability increases indefinitely.

suppressing gradients in $\bar{u}$ that might otherwise continue to grow. We will look at this mechanism in more detail in Section 4.

3. Internal wave model

a. Model equations

We wish to study several aspects of the inertial waves/frontal interaction problem. In Section 2, we showed that inertial oscillations in a surface mixed layer interact with a mean flow through a proliferation of ever-decreasing wavelengths. When we dynamically couple the mixed layer with a stratified interior, inertial waves disperse into the interior and retard this proliferation of length scales.

In order to study this coupling mechanism, we formulate a model with a well-mixed surface layer of varying depth h, and a stratified interior with no turbulent mixing. Figure 4 schematically portrays the model configuration. We measure z downwards from the surface, and we confine attention to two spatial dimensions, with all functions independent of y. We assume a flat bottom at $z = D$ and a rigid lid at $z = 0$.

We scale out a reference density and hydrostatic

pressure gradient from the vertical momentum equation, and assume a hydrostatic balance,

$$\frac{\partial p}{\partial z} = -b, \tag{3.1}$$

where b is the upward buoyancy acceleration. The full Boussinesq equations for the surface mixing layer are

$$h\left(\frac{\partial \bar{u}}{\partial t} + \bar{u}\frac{\partial \bar{u}}{\partial x} - f\bar{v} + \frac{\overline{\partial p}}{\partial x}\right) = \tau_x,$$

$$h\left(\frac{\partial \bar{v}}{\partial t} + \bar{u}\frac{\partial \bar{v}}{\partial x} + f\bar{u}\right) = \tau_y,$$

$$h\left(\frac{\partial \bar{b}}{\partial t} + \bar{u}\frac{\partial \bar{b}}{\partial x}\right) = B_s. \tag{3.2a–c}$$

Here, overbars indicate depth-averaging over the mixed layer. The surface wind stress has components τ_x and τ_y, and B_s is the surface buoyancy flux due to net heating and net rainfall, always taken as zero. From the hydrostatic condition,

$$p = p(h) + (h - z)\bar{b}. \tag{3.3}$$

Therefore the depth-averaged pressure gradient is

$$\frac{\overline{\partial p}}{\partial x} = \frac{\partial p(h)}{\partial x} + \frac{h}{2}\frac{\partial \bar{b}}{\partial x} + \bar{b}\frac{\partial h}{\partial x}. \tag{3.4}$$

The layer thickness changes with the divergence of momentum transport within the layer,

$$\frac{\partial h}{\partial t} = -\frac{\partial}{\partial x}(\bar{u}h). \tag{3.5}$$

The interior equations are

$$\frac{\partial u}{\partial t} + u\frac{\partial u}{\partial x} + w\frac{\partial u}{\partial z} - fv = -\frac{\partial p}{\partial x},$$

$$\frac{\partial v}{\partial t} + u\frac{\partial v}{\partial x} + w\frac{\partial v}{\partial z} + fu = 0,$$
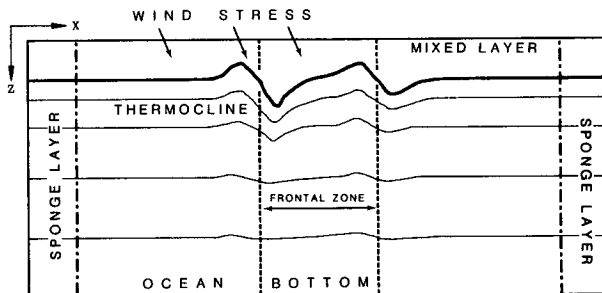

FIG. 4. Schematic diagram of the computational domain of the numerical model. The components are not drawn to scale. The thick solid curve represents the base of the mixed layer. The thin solid curves take on similar shapes, and represent some of the ζ levels.

$$\frac{\partial b}{\partial t} + u\frac{\partial b}{\partial x} + w\frac{\partial b}{\partial z} = 0,$$

$$\frac{\partial u}{\partial x} + \frac{\partial w}{\partial z} = 0,$$

$$\frac{\partial p}{\partial z} = -b. \qquad (3.6\text{a-e})$$

The required boundary conditions are pressure continuity at the interface $z = h$, and

$$w = 0$$

at the bottom. The continuity of w at the interface is ensured by the condition of zero total flux in the x-direction,

$$h\bar{u} + \int_h^D u\,dz = 0. \qquad (3.7)$$

This condition determines the interface pressure distribution $p(x, h, t)$, apart from an arbitrary added function of time.

b. Initial steady state

We assume an initial steady-state solution representing a frontal jet near $x = 0$. This solution is denoted using upper case variables. We take the steady-state interface depth

$$H = \text{constant}, \qquad (3.8)$$

and zero current in the x-direction

$$U = \bar{U} = 0. \qquad (3.9)$$

We use a barotropic (depth independent) formulation for the frontal jet, $\bar{V}(x) = V(x)$, given by (2.5) and shown in Fig. 1. In the interior, the steady-state momentum and hydrostatic relations are

$$fV = \frac{\partial P}{\partial x}, \qquad (3.10)$$

$$B = -\frac{\partial P}{\partial z}. \qquad (3.11)$$

Therefore,

$$P = P_0(z) + f\int V dx, \qquad (3.12)$$

$$B = -\frac{dP_0}{dz}. \qquad (3.13)$$

For simplicity, we take a uniform Väisälä frequency N_0. By definition,

$$N_0^2 = -\frac{\partial B}{\partial z}, \qquad (3.14)$$

and combining (3.13), (3.14) we get

$$P_0(z) = N_0^2 \frac{z^2}{2}. \qquad (3.15)$$

For the surface layer,

$$\bar{B} = \frac{P_0(0) - P_0(H)}{H} = \frac{1}{2}N_0^2 H. \qquad (3.16)$$

The implication of (3.16) is that $\bar{B}$ is constant in time and space.

c. Equations for a small disturbance

We assume a small disturbance to the basic state solution and replace v in the equations by $V + v$. We replace the other equations similarly, except for h, for convenience. We then selectively drop nonlinear terms.

We do not explicitly include wind stress or surface buoyancy flux. Therefore, we let $\tau_x = \tau_y = B_s = 0$. From (3.2c) it follows that $\bar{b}$ is constant in space and time, and (3.4) becomes

$$\frac{\overline{\partial p}}{\partial x} = \frac{\partial p(h)}{\partial x} + \bar{b}\frac{\partial h}{\partial x}. \qquad (3.17)$$

In the mixed layer,

$$\frac{\partial \bar{u}}{\partial t} - f\bar{v} = -\frac{\overline{\partial p}}{\partial x}, \qquad (3.18)$$

$$\frac{\partial \bar{v}}{\partial t} + f\bar{u} + \bar{u}\frac{\partial \bar{V}}{\partial x} = 0. \qquad (3.19)$$

The equation for the interface is

$$\frac{\partial h}{\partial t} = -\frac{\partial}{\partial x}(\bar{u}h). \qquad (3.20)$$

In the interior,

$$\frac{\partial u}{\partial t} - fv = -\frac{\partial p}{\partial x}, \qquad (3.21)$$

$$\frac{\partial v}{\partial t} + fu + u\frac{\partial V}{\partial x} = 0, \qquad (3.22)$$

$$\frac{\partial b}{\partial t} + w\frac{\partial B}{\partial z} = 0, \qquad (3.23)$$

$$\frac{\partial u}{\partial x} + \frac{\partial w}{\partial z} = 0, \qquad (3.24)$$

$$\frac{\partial p}{\partial z} = -b. \qquad (3.25)$$

In addition,

$$w = 0 \quad \text{at} \quad z = D, \qquad (3.26)$$

$$\bar{u}h + \int_h^D u\,dz = 0. \qquad (3.27)$$

d. Method of solution

We solve the model equations numerically, using a finite difference scheme. We introduce computational boundaries at $x = \pm X$, and apply the artificial boundary conditions

$$\frac{\partial b}{\partial t} + c\frac{\partial b}{\partial x} = 0, \qquad (3.28)$$

with corresponding conditions for h. Here c is a nominal phase speed for the waves reaching the boundary, and is positive on the right, and negative on the left.

This method was applied successfully by Price (1983). There is a problem though, in that the phase speed c is not constant in time. Different vertical modes arrive at the side boundaries with different phase speeds. The lowest mode arrives at the sides most swiftly, with the fastest phase speed. We set c approximately equal to the phase speed of the lowest vertical modes. Higher mode waves have slower phase speeds, and therefore are not handled well by (3.28).

To alleviate this problem, a sponge was implemented along both of the side boundaries. We added the terms $-\sigma_u u$, $-\sigma_u v$, and $-\sigma_b b$ to the prognostic equations for u, v, and b (3.21, 3.22, 3.23), respectively. The formulations for σ_u and σ_b are

$$\begin{Bmatrix} \sigma_u(r) \\ \sigma_b(r) \end{Bmatrix} = \begin{Bmatrix} \hat{\sigma}_u \\ \hat{\sigma}_b \end{Bmatrix} \exp[-\sinh(\sinh r/\Gamma)], \qquad (3.29)$$

where r is the lateral distance from a side wall and Γ characterizes the thickness of the porosity distribution. This formulation was also used by Rubenstein (1983). This sponge technique reduces the energy of higher modes of internal waves. The higher modes propagate slowly, and therefore spend more time in the porosity distribution, becoming extinguished. This method, therefore, complements the radiation boundary condition technique, which is tuned to the lowest modes.

We transform z, in the interval $h(x, t)$ to D, to the variable ζ, in the interval from 0 to M. We then take finite differences with unit spacing to represent derivatives with respect to ζ. The transformation is defined by the equation

$$\frac{\partial z}{\partial \zeta} = \beta(\alpha + \zeta)^{1/2}, \qquad (3.30)$$

which we regard as optimal, where $\alpha = \frac{1}{2}$ is a constant used to control the relative spacing near the interface, and

$$\beta = \frac{3}{2}\left[\frac{D - h}{(\alpha + M)^{3/2} - \alpha^{3/2}}\right]. \qquad (3.31)$$

The required dependence on $\alpha + \zeta$ was derived on theoretical grounds that are not presented here in detail. Briefly, the vertical group velocity decreases with the vertical length scale, so that the shortest length scales can only propagate a short distance into the interior during our computational period. For the computations discussed here, $M = 35$. For longer computations, larger values of M should be used, with values of α up to order M.

In the equations, the derivatives with respect to x and t are at constant z. The required transformations for a function $f(x, z)$ to (x, ζ) coordinates are

$$\frac{\partial f}{\partial t} \rightarrow \frac{\partial f}{\partial t} + \frac{\partial \zeta}{\partial t}\frac{\partial f}{\partial \zeta},$$

$$\frac{\partial f}{\partial x} \rightarrow \frac{\partial f}{\partial x} + \frac{\partial \zeta}{\partial x}\frac{\partial f}{\partial \zeta},$$

$$\frac{\partial f}{\partial z} \rightarrow \frac{\partial \zeta}{\partial z}\frac{\partial f}{\partial \zeta}.$$

The finite difference grid is staggered in space. In the vertical, w and b are defined at integer values of ζ, and u, v, and p at half-integer values. In the horizontal, u and v are defined along the columns $n\delta x$, where $n = 1, 2, \cdots, L$, and w, b, and p along the columns $(n + 1/2)\delta x$ for $n = 0, 1, 2, \cdots, L$. Spatial derivatives are center-differenced.

During each time step, the following integration algorithm is performed:

1) The new mixed layer depth is computed using (3.20).
2) The vertical coordinate ζ and its derivatives $\partial\zeta/\partial z$, $\partial\zeta/\partial x$, $\partial\zeta/\partial t$ are computed.
3) The hydrostatic Eq. (3.25) is integrated for pressure.
4) The continuity Eq. (3.24) is integrated for w, using the boundary condition (3.26).
5) Mixed layer variables $\bar{u}$, $\bar{v}$ are stepped forward using (3.18), (3.19).
6) Interior variables u, v, b are stepped using (3.21)–(3.23).
7) A pressure adjustment $\Delta p(x)$ is computed, in order to satisfy the constraint in (3.27).

The first time step is performed using a simple Euler step, and succeeding steps use a leap-frog scheme. The time step is 300 s for all model runs. In order to avoid time splitting, a special precaution is taken. At each time step, the maximum amplitude of $|\partial^2 u/\partial t^2|$ is calculated. When this amplitude changes by more than 50% with respect to the previous time step, then two pairs of succeeding time steps are averaged. Then the leap-frog scheme is resumed.

e. Model parameters

The values of model parameters are as follows:

1) Initial values

$$H = 50 \text{ m}$$

$$u = v = b = w = 0$$

$$\bar{u} = \bar{b} = 0$$

$$\bar{v} = 20 \text{ cm s}^{-1}$$

2) Ocean front parameters

$$\lambda = 80 \text{ km}$$

$$V_0 = 15 \text{ cm s}^{-1}$$

3) Model geometry

$$f = 10^{-4} \text{ s}^{-1}$$

$$N_0 = 3 \text{ cph}$$

$$D = 4 \text{ km}$$

Total extent $-X < x < X$; $X = 300$ km

$$\delta t = 300 \text{ s}$$

Horizontal grid = 62 points

Vertical grid $M = 35$ points

4) Porosity distribution

$$\sigma_u = \sigma_b = 1.2 \times 10^{-5} \text{ s}^{-1}$$

$$\Gamma = 150 \text{ km}.$$

4. Model results

In this section we solve the model equations presented in Section 3. We initialize the numerical integration with a homogeneous perturbation flow $(\bar{u}, \bar{v})$ = $(0, \bar{v}_0)$ in the mixed layer.

In analyzing near-inertial oscillations from current meter observations, it is often desirable to perform a complex demodulation. This technique is useful for interpreting model results, as well. In essence, complex demodulation involves multiplying a complex-valued time series $u(t) + iv(t)$ by a unit-magnitude complex vector $\exp(ift)$, and then applying an appropriate low pass filter. By computing the amplitude of the resultant complex time series, we obtain the time-dependent amplitude, or speed, of the near-inertial oscillations.

Figure 5 shows the speed of the near-inertial oscillations in the mixed layer. Most of the variability occurs inside or near the ocean front region, $40 \lessapprox x \lessapprox 40$ km. Inside this region oscillations decay quite rapidly. The near-inertial energy in the frontal region is associated with short horizontal wavelengths, and therefore is able to propagate rapidly into the interior. The initial amplitude is 20 cm s^{-1}. Within ten inertial periods, at $x \sim 15$ km, the inertial amplitude decays to less than 3 cm s^{-1}, and then increases again. On the negative vorticity (left) side of the ocean front, the inertial amplitude initially increases to 21 cm s^{-1}, and then decays to less than 6 cm s^{-1}, but at a slower rate than on the positive vorticity side.

The decay of inertial amplitude is more rapid on the positive vorticity (right) side of the front, than on the negative vorticity side. This asymmetry results from the more rapid internal wave dispersion for waves originating on the positive vorticity side. To understand this argument, we use a qualitative ray tracing approach. From (3.21)–(3.25), the dispersion relation is

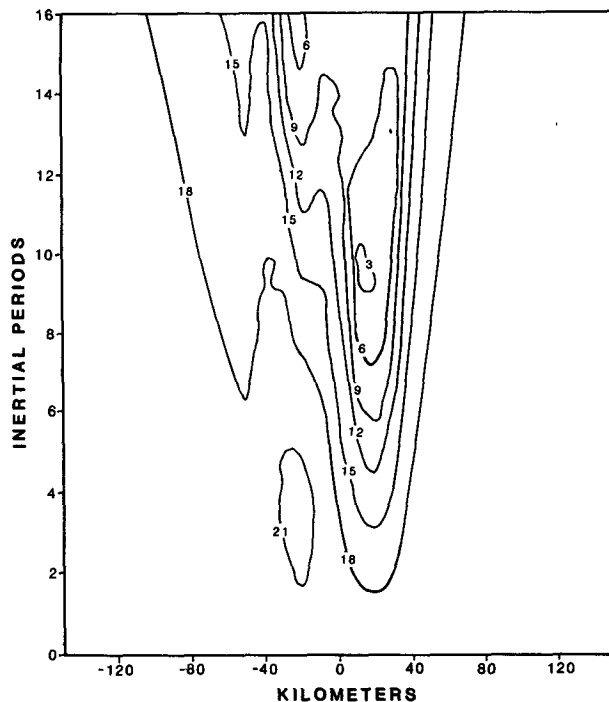$$\omega^2 = f_e^2 + \left(\frac{k_x N}{k_z}\right)^2, \tag{4.1}$$

Fig. 5. Speed of inertial oscillations in the mixed layer. The contour increment is 3 cm s^{-1}. Initial speed is 20 cm s^{-1}.

where ω is angular frequency, f_e the effective inertial frequency, and k_x and k_z are the horizontal and vertical wavenumbers. Lighthill (1978) showed that, in the absence of an explicit time dependence, frequency is constant along the ray traced by a propagating wave. In our present case, N is a constant, and $f_e(x)$ is given by (2.4), (2.5), and shown in Fig. 1. Therefore k_x varies along a propagation ray, while k_z is constant. As we follow a wave originating at the peak in f_e (at $x = 20$ km), its wavenumber k_x increases to balance out the decrease in f_e. Therefore, the magnitudes of both the horizontal and vertical components of group velocity,

$$(C_x, C_z) = \left(\frac{N}{k_z}\right)^2 \frac{k_x}{\omega}\left(1, -\frac{k_x}{k_z}\right), \tag{4.2}$$

increase along the ray. In contrast, the magnitudes of the group velocity components decrease following a wave originating at the trough of f_e (at $x = -20$ km).

Figures 6a, b show the inertial amplitudes at 200 and 800 m depth. Each successive depth exhibits weaker and more dispersed structure. At both of these depths, most of the energy is distributed on the negative vorticity (left) side of the front. These results are similar to theoretical results reported by Kunze (1985) and Kunze and Sanford (1984). They found a tendency for near-inertial waves to reflect or refract away from the positive vorticity side of an ocean front. Also, certain waves were trapped within the negative vorticity side of a front. Our results also show a tendency toward
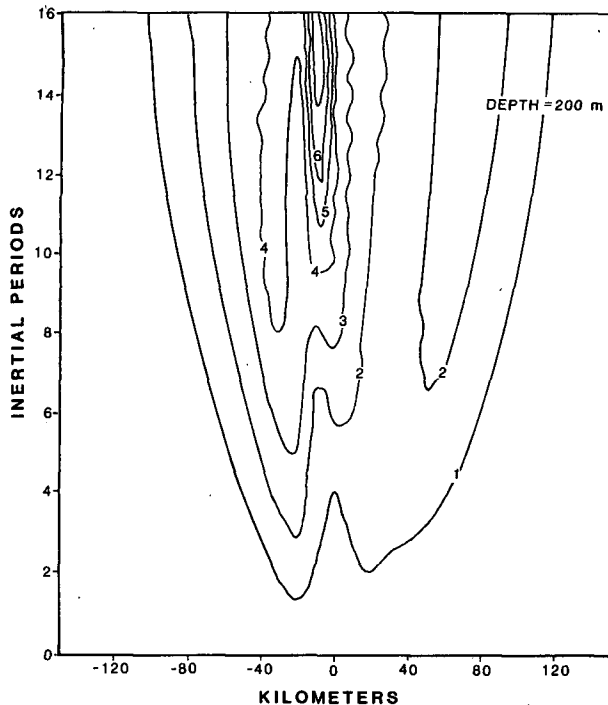
FIG. 6a. Speed of inertial oscillations at the depth $z = 200$ m. Contour increment is 1 cm s^{-1}.

trapping, especially in the upper 400 m of the thermocline. However, the trapping is only partial; much of the inertial energy escapes from the negative vorticity trough. This can be seen more clearly in Fig. 7, which shows a cross section of $u(x, z)$ in the upper 800 m, after 13.3 inertial periods. There is a relative concentration of energy density in the negative vorticity region and a relative depletion in the positive vorticity region.

Figure 8 shows contours of mixed layer depth perturbations $h(x, t) - H$. The amplitudes of these perturbations increase at a slower rate than those shown in Fig. 3. The perturbation amplitude in the negative vorticity region $-40 < x < 0$ km increases at half the rate as in Fig. 3, while the perturbation amplitude in the positive vorticity region $0 < x < 40$ km increases much more slowly. As a result, there is a marked asymmetry present in Fig. 8.

Moreover, the mixed layer depth perturbations do not increase indefinitely, as they do in Fig. 3. The dispersion of inertial energy reduces the gradients of momentum transport in the mixed layer. From (3.20), therefore, variability in h increases at a slower rate. The asymmetry in Fig. 8 results from the faster dispersion of waves originating in the positive vorticity region.

5. Summary and discussion

The purpose of this paper is to suggest a possible mechanism for the scattering of near-inertial internal

waves by an ocean front. The scattering mechanism depends on the existence of a mean flow that may accompany a front. The vorticity of this mean flow alters the effective inertial frequency. Even if inertial oscillations in the vicinity of the front are initially coherent, they eventually lose their coherence, due to local variability of the effective inertial frequency. The oscillations gradually accumulate a phase shift across the front, resulting in strong horizontal gradients in the horizontal velocity, and strong inertial pumping. The inertial pumping has spatial scales on the order of half the frontal width—a few tens of kilometers—and gives rise to the following three effects:

a. Inertial amplitudes

Inertial pumping generates internal waves that propagate downward and away from the front. Radiation damping selectively removes near-inertial energy from the front and its vicinity. Within ten inertial periods, the inertial amplitude can decrease by 85% in the positive vorticity region of the mixed layer.

b. Wave dispersion

In the thermocline, inertial energy rapidly disperses away from the positive vorticity side of the front. Waves disperse more slowly from the negative vorticity side, and have shorter horizontal wavelengths. There is a tendency toward partial trapping in the thermocline, above 400 m.
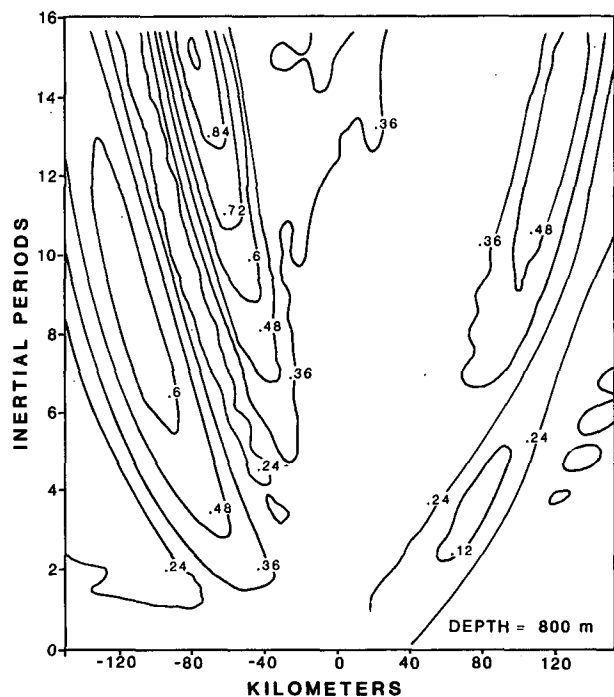

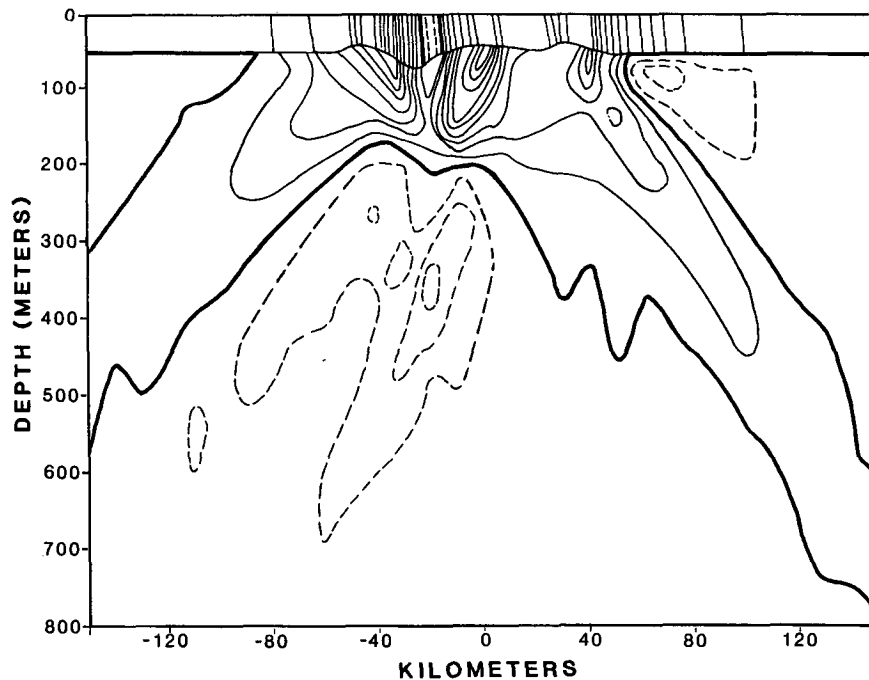FIG. 6b. As in (a) but at $z = 800$ m. Contour increment is 0.12 cm s^{-1}.

FIG. 7. Cross section of model prediction of $u(x, z)$ at time $t = 13.3$ inertial periods. Only the upper 800 m are shown. Solid (dashed) curves denote positive (negative) velocities. The thick curves denote zero contours. The contour increment is 1 cm s^{-1}.

c. Mixed layer depth

Inertial pumping causes the mixed layer depth to oscillate. Nonlinear advection becomes important if inertial oscillations in the mixed layer are sufficiently strong (so that a fluid element traverses across a significant fraction of the horizontal scale of variability within an inertial period). Then the mixed layer depth alters cumulatively. The net result is a strong cross-front variability in mixed layer depth. The variability is particularly strong in the negative vorticity region, where the layer can deepen from 50 to 78 m within 16 inertial periods.

Some of the theoretical findings are suggestive of the observations made by Kunze and Sanford (1984). They found strong variability of near-inertial energy across the North Pacific Subtropical Front. A sharp peak in downward propagating energy was observed on the warm side of the front, some four times stronger than the background level. Kunze and Sanford computed the dropped, rotated, horizontal coherence magnitude and phase versus horizontal separation for the 128 m vertical wavelength, clockwise-with-depth Fourier component. Oscillations in the real part of the coherence, and three consecutive zero-crossings of the phase were suggestive of cross-frontal variability, with a 30 km wavelength. By excluding different parts of the dataset and recalculating the coherence, they found that the wavelike structure was limited to the negative vorticity side of the front.

This structure resembles the model result shown in Fig. 6b. Most of the variability occurs on the (left) negative vorticity side of the front. This asymmetry results from the shorter horizontal wavelengths—and hence the slower energy propagation—of waves originating in the negative vorticity region of the front.

The results of this study are consistent with observations in the California Current system by Pinkel (1983) and by Weller (1985). Using a Doppler sonar instrument deployed from FLIP, Pinkel found that on average, near-inertial energy propagation was predominantly downward. In addition, he observed at least three distinct wave packets. Two of these packets were propagating downward, and one upward. Vertical wavelengths ranged from 125 to 500 m, and horizontal wavelengths from 8.5 to 25 km. These horizontal wavelengths are smaller than expected from wind generated waves in a horizontally uniform ocean. Weller (1985) analyzed data from current meters deployed from FLIP concurrently with Pinkel's Doppler sonar experiment. Using a simple model, Weller showed that local meteorological forcing alone could not explain the strength and variability of the observed near-inertial velocity variability in the mixed layer. He attributed much of this apparent temporal variability to small scale spatial variability of the fields through which FLIP drifted. He noted that horizontal shears in the region are known to be quite strong—comparable to those of our model front. In addition, three periods of intensified inertial amplitude were associated with regions
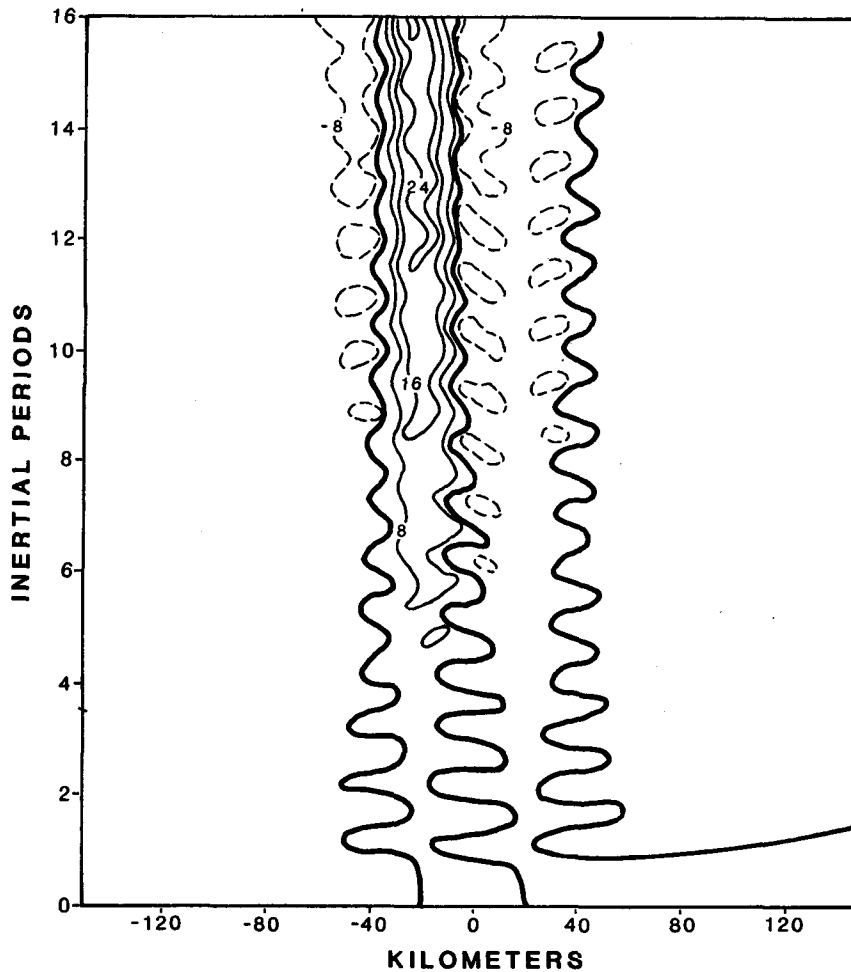
FIG. 8. Mixed layer depth perturbations $h(x, t) - H$, where $H = 50$ m. The contour increment is 8 m. The thick curves indicate zero contours. Dashed curves denote negative perturbations.

of horizontal shear and rapid temperature changes. However, a fourth period of inertial amplification was not associated with a large temperature change. This finding is consistent with our model results. Inertial energy tends to be partly scattered away from a front, in addition to being partly trapped. Therefore, we may expect to find regions of inertial intensification not only inside the negative vorticity trough of a front (as discussed by Kunze and Sanford, 1984) but also away from, but in the vicinity of a front.

Rubenstein (1983) and Gill (1984) showed that the rate of inertial energy dissipation in the mixed layer depends strongly on the horizontal scales of the waves. For a wave that is periodic in space, Gill found that the time scale over which a vertical mode separates in phase by 90° from a pure inertial oscillation is approximately proportional to its horizontal wavelength, squared. However, due to the beating of modes and pure inertial oscillations, the amplitude in the mixed layer does not dissipate monotonically. Inertial energy periodically returns to the mixed layer. For a spatially periodic wave, vertical dispersion is not particularly efficient for radiating energy. This is the case for motions induced by a synoptic-scale storm over a homogeneous (f-plane) ocean.

In contrast to periodic waves, laterally bounded waves radiate energy more efficiently. Lateral dispersion allows energy to radiate away, never to return. Gill (1984) showed that the time scale for a wave mode to propagate across a bounded storm track is proportional to its wavelength, squared. The waves simulated in the present study are similar, in the sense that their source is bounded. Lateral dispersion reduces the inertial energy in the mixed layer, primarily in the front, but also in regions just adjacent to it. This reduction occurs on both sides of a mean flow, especially on the side of positive vorticity. Because near-surface fronts are ubiquitous in many ocean regions, the mechanism postulated in this paper may have profound implications for the distribution of near-inertial energy.

REFERENCES

Fu, L. L., 1981: Observations and models of inertial waves in the deep ocean. *Rev. Geophys. Space Phys.,* **19,** 141–170.

Gill, A. E., 1984: On the behavior of internal waves in the wakes of storms. *J. Phys. Oceanogr.,* **14,** 1129–1151.

Kunze, E., 1985: Near-inertial wave propagation in geostrophic shear. *J. Phys. Oceanogr.,* **15,** 544–565.

——, and T. B. Sanford, 1984: Observations of near-inertial waves in a front. *J. Phys. Oceanogr.,* **14,** 566–581.

Lighthill, J., 1978: *Waves in Fluids.* Cambridge University Press, 504 pp.

Mied, R. P., C. Y. Shen, C. L. Trump, and G. J. Lindemann, 1985: Internal-inertial waves in a Sargasso Sea front. Submitted to *J. Phys. Oceanogr.*

Pinkel, R., 1983: Doppler sonar observations of internal waves: Wavefield structure. *J. Phys. Oceanogr.,* **13,** 804–815.

Pollard, R. T., 1980: Properties of near-surface inertial oscillations. *J. Phys. Oceanogr.,* **10,** 385–398.

Price, J. F., 1983: Internal wave wake of a moving storm. Part I: Scales, energy budget and observations. *J. Phys. Oceanogr.,* **13,** 949–965.

Rubenstein, D. M., 1983: Vertical dispersion of inertial waves in the upper ocean. *J. Geophys. Res.,* **88,** 4368–4380.

Schott, F., 1971: Spatial structure of inertial-period motions in a two-layered sea, based on observations. *J. Mar. Res.,* **29,** 85–102.

Webster, F., 1968: Observations of inertial-period motions in the deep sea. *Rev. Geophys.,* **6,** 473–490.

Weller, R. A., 1982: The relation of near-inertial motions observed in the mixed-layer during the JASIN (1978) experiment to the local wind stress and to the quasigeostrophic flow field. *J. Phys. Oceanogr.,* **12,** 1122–1136.

——, 1985: Near surface velocity variability at inertial and subinertial frequencies in the vicinity of the California Current. *J. Phys. Oceanogr.,* **15,** 372–385.